

Effect of Salinity on Effective CO₂ Permeability in Reservoir Rock Determined by Pressure Transient Methods: an Experimental Study on Hawkesbury Sandstone

T. D. Rathnaweera · P. G. Ranjith ·
M. S. A. Perera

Received: 30 June 2014 / Accepted: 24 October 2014 / Published online: 12 November 2014
© Springer-Verlag Wien 2014

Abstract The determination of effective carbon dioxide (CO₂) permeability in reservoir rock and its variation is of great interest in the process of CO₂ sequestration in deep saline aquifers, as CO₂ sequestration-induced permeability alternations appear to create major problems during the CO₂ injection process. The main objective of this study is to investigate the effect of salinity on the effective CO₂ permeability of reservoir rock under different injection pressures. A series of high-pressure tri-axial experiments was, therefore, performed to investigate the effect of salinity on effective CO₂ permeability in Hawkesbury sandstone under various brine concentrations. The selected brine concentrations were 0, 10, 20, and 30 % sodium chloride (NaCl) by weight and the experiments were conducted for a range of CO₂ injection pressures (2, 4, 6, 8, 10, and 12 MPa) at a constant confinement of 20 MPa and a temperature of 35 °C, respectively. According to the results, the degree of salinity of the aquifer's pore fluid plays a vital role in the effective CO₂ permeability variation which occurs with CO₂ injection, and the effective permeability decreases with increasing salinity in the range of 0–30 % of NaCl. Interestingly, in dry reservoir rock samples, the phase transition of the injection of CO₂ from gas to super-critical condition caused a sudden reduction of CO₂ permeability, related to the slip flow effect which occurs in gas CO₂. Transfer into vapor or super-critical CO₂ causes this slip flow to be largely reduced, reducing the reservoir permeability for CO₂ movement in dry reservoir rock samples. However, this behavior was not

observed for water- and brine-saturated samples, and an increasing trend of effective CO₂ permeability was observed with increasing injection pressure. A detailed chemical analysis was then conducted to understand the physical phenomenon causing the salinity effect on effective CO₂ permeability using scanning electron microscopy analyses. Such analyses explain the reason for the observed permeability variations by giving detailed images of the rock sample's microstructure. There were clear depositions of NaCl crystals in the rock's pore space, and the amount increased with increasing brine concentration.

Keywords CO₂ sequestration · Saline aquifers · Effective CO₂ permeability · Salinity · Effective stress

1 Introduction

According to existing studies, deep saline aquifers are the most effective geological formation for CO₂ geo-sequestration, and seams located at 800–2,000 m depths which are highly saline ($\approx 20,000$ and $250,000$ mg/l) are most preferable, (Bachu and Bennion 2008). However, both CO₂ injection and storage capacities in saline aquifers are largely dependent on its permeability. According to past studies, permeability of sedimentary rocks in saline aquifers may vary significantly, depending on the rock formation properties and its depth (Neuzil 1994; Wang 2000). Injection of CO₂ into a saline aquifer during the sequestration process initiates many complex geo-chemical reactions, which significantly affect aquifer permeability. Due to high pressure and temperature conditions in deep saline aquifers, CO₂ exists in its highly complex and chemically reactive super-critical state, which enhances the process complexity. As a result, the prediction of aquifer

T. D. Rathnaweera · P. G. Ranjith (✉) · M. S. A. Perera
Deep Earth Energy Laboratory, Department of Civil
Engineering, Monash University, Building 60, Melbourne,
VIC 3800, Australia
e-mail: ranjith.pg@monash.edu

permeability during the sequestration process becomes a challenge. According to Hangx et al. (2013) and Mohan et al. (1999), CO₂ injection pressure induces creep and micro-cracking, diffusive mass transfer processes, long-term mineralogical alteration, growth of NaCl crystals in the formation pore structure and fine particle migration in the rock pore space. These are the main factors which alter the aquifer's permeability during the CO₂ sequestration process. Although, the combined effect decides the final permeability variation, in most cases permeability tends to reduce with long-term CO₂ injection (Pearce et al. 1996, White et al. 2003). It is possible that the permeability reducing measures (e.g., NaCl crystallization and mineral depositions mainly clay mineral precipitation) make a greater contribution than the enhancing measures (e.g., cracking and mineral dissolution). However, the fluctuation of reservoir permeability during CO₂ injection is by no means favorable, as it causes the aquifer's storage capacity to decrease (Ranjith et al. 2013) and CO₂ injectability into the reservoir to decline, which affect the effectiveness of the whole process. Therefore, high injection pressures are required to maintain the effectiveness of the process. According to Vilarrasa et al. (2010), over-pressured CO₂ injection can cause excessive compression or even tension in the formation, resulting in formation of cracks and fractures (Rutqvist and Tsang 2002), which create leakage pathways for the injected CO₂ to back-migrate into the atmosphere. In spite of these facts, increased pore pressure in the reservoir at higher injection pressures counteracts the overburden pressure that may even cause the ground surface to be uplifted (e.g., the Salah CO₂ storage project) (Arsyad et al. 2013). In addition, lateral movement of the CO₂ plume along the formed fractures can contaminate underground fresh-water aquifers, which is a crucial

environmental impact. Therefore, it is essential to have detailed knowledge of reservoir permeability and its variation during the sequestration process. The main objective of the present study was to obtain such knowledge through (1) a comprehensive literature review and (2) a well-planned experimental programme. Under the experimental programme, the effect of the salinity level of the aquifer on its effective CO₂ permeability was determined under in situ conditions by performing high-pressure tri-axial experiments on samples sourced from the Gosford Basin, Australia. Scanning electron microscopy (SEM) and chemical analysis were also conducted to identify the corresponding interior (mineralogical and micro-logical) structure variation in the aquifer.

2 Literature Review

2.1 Effect of Brine Concentration

Over the last decade, a number of experimental studies on CO₂-brine flow systems in various rocks have been performed using steady and unsteady state tri-axial tests and core-flooding techniques to evaluate the rock permeability variation with CO₂ injection under various test conditions, including different CO₂ injection pressures, temperatures, depths, and salinity levels. The effect of salinity level is the main concern of this study. Table 1 below shows the summary of experimental studies carried out to date on the effect of salinity on effective CO₂ permeability of sandstone. As Table 1 indicates, although understanding of the effect of pore fluid brine concentration on reservoir effective CO₂ permeability is of great interest in environmental engineering, geothermal exploration, and the petroleum

Table 1 Summary of studies on the salinity effects on the permeability of reservoir rocks

Reference	Sample	Used fluids	Confining pressure (bar)	Temperature (°C)	Permeability variation (%)
Aktan and Farouk (1975)	Berea sandstone	NaCl (2 %)	4.1–206	27–260	Decrease
	Boise sandstone	NaCl (2 %)	4.1–206	27–260	N. C
Sydansk (1981)	Berea sandstone fired at 450 °C	NaCl (3 %)	138	22–85	Decrease
Khilar (1981)	Berea sandstone	NaCl: H ₂ O		0; 30; 60	$k_{60} > k_{30} > k_0$
Miller and Ramey (1986)	Berea sandstone	NaCl (22 %)	34	21–93	N. C
		NaCl (2 %)	34	21–93	Decrease
Ochi and Vernoux (1998)	Berea sandstone	NaCl (0.01–0.5 M)	0–250	0–90	Decrease
Bachu and Bennion (2008)	Alberta basin Canada	CO ₂ /brine system	200–2,000	30–50	Decrease
Berg et al. (2013)	Berea sandstone	CO ₂ /brine system	100–300	45	N.C
Samuel et al. (2012)	Berea sandstone Mt. Simon sandstone	CO ₂ /brine system	400–1,000	50	Decrease

industry, to date few related studies are available (Ochi and Vernoux 1998; Kuhn et al. 1998; Bachu and Bennion 2008; Probst 2008; Berg et al. 2013; Ranjith et al. 2013).

Of these studies, that conducted by Probst (2008) found a decreasing trend of aquifer effective CO₂ permeability with increasing brine concentration, and the salt evaporation effect, called the “salting out effect”, was the factor suspected to cause a denser water phase that reduces CO₂ solubility in water. According to Julio (2001), this salting out effect may cause water density to be increased by up to around 20 %, and H₂O–CO₂ interaction may cause this value to be further increased by 2–3 %. Later, Ranjith et al. (2013) studied the effect of salinity on effective CO₂ permeability in saline aquifers with 100,000–160,000 ppm high salinity levels, and confirmed the effective CO₂ permeability reduction with increasing salinity. The estimated total CO₂ storage capacity reduction in their study due to this permeability reduction is up to around 1.8 %.

Although few studies are available related to the effect of brine concentration on effective CO₂ permeability in aquifers, many studies have been conducted on the effect on effective brine permeability (Baudracco and Tardy 1988; Mohan et al. 1999). Mohan et al. (1999) showed the effect of high ionic strength brines on the absolute permeability of smectitic sandstones, and a decreasing trend of effective brine permeability in sandstone with increasing brine concentration was observed. According to these researchers, the corresponding damage, which is the permeability reduction of the host rock due to contact with the foreign fluid, is irreversible (Mohan et al. 1999). According to Baudracco and Tardy (1988), a reservoir’s effective brine permeability decreases with increasing brine concentration for a given cation, and 10 % reduction in permeability in specimens saturated in NaCl, 12 % in NaNO₃, 13 % in Na₂SiO₃, and 16 % in NaOH was observed by Omar (1990). This permeability variation creates permanent changes in the flocculation and deflocculation phases of colloidal clay in reservoir rocks (Baudracco and Tardy 1988). The different ionic concentrations creating variation in host fluid permeability have also been studied by Dahab et al. (1992) using three types of sandstones (Berea, Saudi, and Aramco) under a range of temperatures and pressures. These researchers concluded that the observed permeability reduction is related to both the degree of variation of the pore fluid’s ionic concentration and the nature of the ions. Moreover, Juanes et al. (2006) presented a comprehensive discussion on the relative permeability characteristics of multi-phase systems related to CO₂ sequestration in deep saline aquifers, and demonstrated how the mechanism of relative permeability-induced capillary trapping can be exploited to improve the overall effectiveness of the injection process. According to past studies (Odeh 1959; Bennion and

Bachu 2005; Bachu and Bennion 2008), among the various factors for the effective CO₂ permeability of sandstone in CO₂-brine systems [injection and confining pressures, temperature, interfacial tension (IFT), viscosity ratio, capillary pressure, degree of saturation], IFT has a significant effect on the displacement characteristics of CO₂-brine systems during the CO₂ injection phase (Bachu and Bennion 2008). Bachu and Bennion (2008) conducted a comprehensive experimental study to investigate the effect of IFT between CO₂ and brine on the relative permeability characteristics of reservoir rock and found that effective CO₂ permeability decreases with increasing IFT. The IFT mainly depends on the pressure, temperature, and brine salinity, and it increases with increasing temperature and salinity and decreasing injection pressure (Yang et al. 2005; Chalbaud et al. 2006). According to Bennion and Bachu (2006c, 2010), the viscosity ratio between CO₂ and brine may also play a considerable role in governing the fluid movement through the CO₂-brine system, and increasing the viscosity contrast between CO₂ and brine causes more easy fluid movement.

Wegener and Harpole (2010) and Burton et al. (2009) showed the importance of correctly evaluating the effective CO₂ permeability in deep saline aquifers CO₂ to determine the potential injectivities and eventually to decide the number of injection wells required.

2.2 Existing Reservoir Permeability Evaluation Measures

Although the variation of reservoir rock permeability with effective stress is a well-established fact, the amount of change is highly variable (Jing et al. 1992; Chen et al. 2007). Davies and Davies (1999) introduced a novel model to evaluate the stress effect on reservoir permeability: see Eq. (1).

$$k = k_0 \exp \left[22.2 \left(\frac{\phi}{\phi_0} - 1 \right) \right] \quad (1)$$

$$\phi = (\phi_0 - \phi_r) \exp(5 \times 10^{-8} \sigma'_M) + \phi_r \quad (2)$$

where, k_0 is the zero stress permeability, ϕ is the porosity and ϕ_0 is porosity at zero stress, ϕ_r is the residual porosity and σ'_M is the mean effective stress and can be defined as follows as a function of principle effective stresses:

$$\sigma'_M = \frac{1}{3} (\sigma'_1 + \sigma'_2 + \sigma'_3) \quad (3)$$

where, the principle effective stresses can be calculated using Biot’s effective stress parameters (Biot 1941) as follows:

$$\sigma'_1 = \sigma_1 + \alpha P \quad (4)$$

$$\sigma'_2 = \sigma_2 + \alpha P \quad (5)$$

$$\sigma'_3 = \sigma_3 + \alpha P \quad (6)$$

where α is Biot's effective stress parameter and P is an average pore pressure, defined as follows:

$$P = S_1 P_1 + (1 - S_1) P_g \quad (7)$$

where S_1 is the degree of liquid saturation, P_1 is the liquid partial pressure, and P_g is the gas partial pressure in the pore fluid. According to Davies and Davies (1999), there can be a one order of magnitude reduction in permeability with the increase of effective stress from zero to 30 MPa. This developed relation was then successfully applied in a numerical simulation developed by Rutqvist and Tsang (2002) to examine the hydro-mechanical changes in reservoir rock due to geo-sequestration of CO₂. The researchers observed proportionally changing aquifer and cap rock permeability values with the effective stress applied to the formation.

Understanding the theory behind fluid flow behavior in reservoir rocks is important to find appropriate solutions to the problems raised in the CO₂ geo-sequestration process in deep saline aquifers. Leverett (1940) developed such a basic theory, combining thermodynamic theories with basic physics, and performed the first experiments to correlate the basic effective factors: saturation, capillary pressure, IFT, and permeability. The capillary pressure function developed by Davies and Davies (1999) was then modified as follows:

$$P_c = P_{co}(S_1) \frac{\sqrt{\frac{k_0}{\Phi_0}}}{\sqrt{\frac{k}{\Phi}}} \quad (8)$$

where, k_0 is the zero stress permeability, Φ is the porosity, Φ_0 is porosity at zero stress, S_1 is the liquid saturation, P_c is the confining pressure, and P_{co} is the initial confining pressure. According to Eqs. (2) and (8), it is clear that the mean stress field greatly influences all the rock flow parameters in saline aquifers; porosity, permeability, and capillary pressure. Later, this phenomena was successfully used by researchers to find the long-term safety of the geo-sequestration process in saline aquifers (failure of the cap rock) by checking the critical pressure, which induces shear slip in pre-existing faults (Rutqvist and Tsang 2002).

Scheidegger (1958) proposed an equation to estimate the reservoir rock permeability for compressible gas flow under steady-state conditions (constant flow rate, Q and a constant hydraulic gradient) as follows:

$$k = \frac{2Q\mu_g L P_d}{A(P_u^2 - P_d^2)} \quad (9)$$

where k denotes the permeability, μ_g represents the viscosity coefficient of the gas, L and A are the length and cross-sectional area of the core sample, and P_u and P_d are the pore air pressure and atmospheric pressure. Later, Dong et al. (2010) used this permeability function to evaluate the stress-dependent permeability and porosity of sedimentary rocks and showed that the intrinsic permeability is independent of the pore fluid. These researchers proposed that rock permeability for gas or water flow should be identical. However, many laboratory experiments have exhibited a greater difference between gas and liquid permeability through porous rocks, where permeability to gas is higher than that to water (Tanikawa and Shimamoto 2009; Faulkner and Rutter 2000). This implies the importance of correctly identifying the difference between gas and water permeability behavior in rocks, especially when considering gas-fluid two-phase systems.

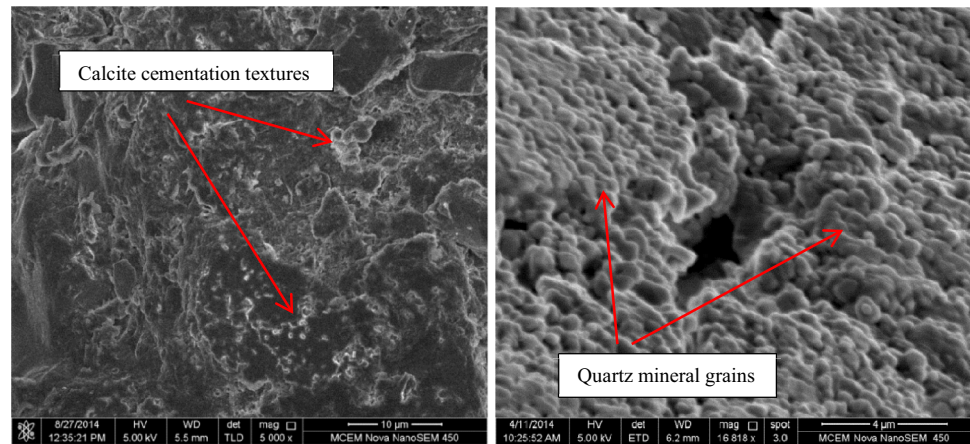
2.3 Klinkenberg Effect for Gas Permeability Measurement

The Klinkenberg effect is one of the best ways to explain the difference between gas and water permeability in porous media. Klinkenberg (1941) discovered that permeability to gas is relatively higher than that to water and explained the reason by introducing a new phenomenon called the "slip flow" effect. The slip flow is the additional flux which occurs due to the collision of gas molecules and solid walls, when a pore radius approaches the mean free path of gas molecules. This significantly enhances the flow rate and is called the Klinkenberg effect (Eq. 10). This phenomenon explains the difference between intrinsic permeability and apparent permeability in porous media, where intrinsic permeability is independent of fluid properties but apparent permeability is a function of both medium and fluid properties. Therefore, although the intrinsic permeability measured for any gas as liquid movement in porous media is the same, apparent permeability may vary with the fluid type. The relationship between the intrinsic and apparent permeability can be given as follows:

$$K_a = \frac{k_i \rho g}{\eta} \quad (9)$$

where, k_i is apparent permeability (m/s), k_i is intrinsic permeability (m²), η is viscosity of fluid (Pa.s), ρ is fluid density (kg/m³), and g is gravitational acceleration (m²/s).

$$k_a = k_i \left(1 + \frac{4cl}{r} \right) = k_i \left(1 + \frac{cKT}{\pi\sqrt{2}r^3 P} \right) = k_i \left(1 + \frac{b}{p} \right) \quad (10)$$

Fig. 1 SEM images of studied sandstone topography

$$b = \frac{cKT}{\pi\sqrt{2}r^3} \quad (11)$$

$$l = \frac{KT}{4P\pi\sqrt{2}r^2} \quad (12)$$

where k_a is the apparent permeability, k_i is the intrinsic permeability, l is the length of the mean free path of the gas molecules, r is the Boltzmann's constant, T is the temperature, c is a constant, P is the pore pressure, and b is the Klinkenberg slip factor. Later, Tanikawa and Shimamoto (2009) measured the permeability of sedimentary rocks taken from the Western Foothills of Taiwan, using nitrogen gas and distilled water as pore fluids under various effective pressure conditions. These researchers observed significantly higher gas permeability values compared to water permeability, and the discrepancy was mainly due to the Klinkenberg effect. They also took an important further step to check the effect of pore pressure on this Klinkenberg effect, and found that although the permeability to gas linearly increases with decreasing pore pressure, water permeability does not have such a linear relationship.

3 Experimental Program

3.1 Sample Preparation

The Hawkesbury sandstone samples were collected from the Gosford quarry in the Sydney basin, Australia and belong to the early Triassic age (Ward 1972). The tested sandstone has a grain size between 0.04 and 1.0 mm with a predominantly argillaceous matrix. The XRD results illustrate that the mineral composition of this dry sandstone includes 85 % quartz, 5 % calcite, 1 % siderite, 1 % mica, 5 % kaolinite, 2 % anatase, and 1 % amphibole, and the main cementing phases consist of quartz, calcite, and kaolinite. Figure 1 below shows the topography of a typical

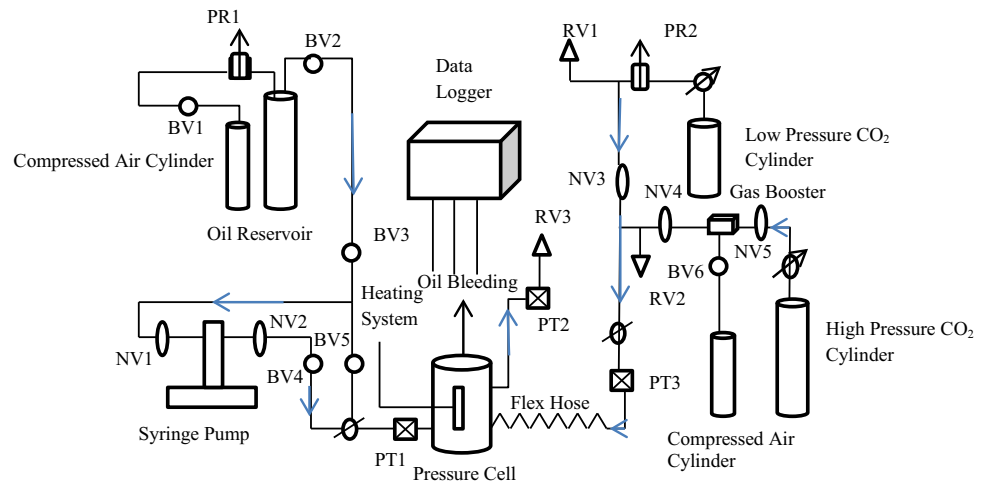
sandstone sample that clearly shows the existing quartz grain and the calcite and kaolinite cementing phase.

The Hawkesbury sandstone samples were cored into 76 mm long and 38 mm diameter cylindrical samples in the Deep Earth Energy Laboratory at Monash University. The top and bottom ends of the samples were then carefully ground to ensure uniform gas injection during the experiments. The prepared samples were oven-dried at 35 °C for 48 h to remove the water added into the pore space during the coring process (during the coring, constant water flow was used to soften the sandstone blocks). All the samples were then saturated using water and brine, with the exception of the two dry samples (at 35 °C), which were used to determine the CO₂ permeability under dry conditions. Two distilled water-saturated samples were used as control samples and the remaining samples were subjected to brine saturation, under three different NaCl concentrations, 10, 20, and 30 % (by weight), to investigate the effect of salinity level on CO₂ injection. Saturation was performed inside desiccators under vacuum for 6 months to achieve full saturation and two replicates were tested for each saturation condition.

3.2 The Tri-Axial Apparatus and Experimental Procedure

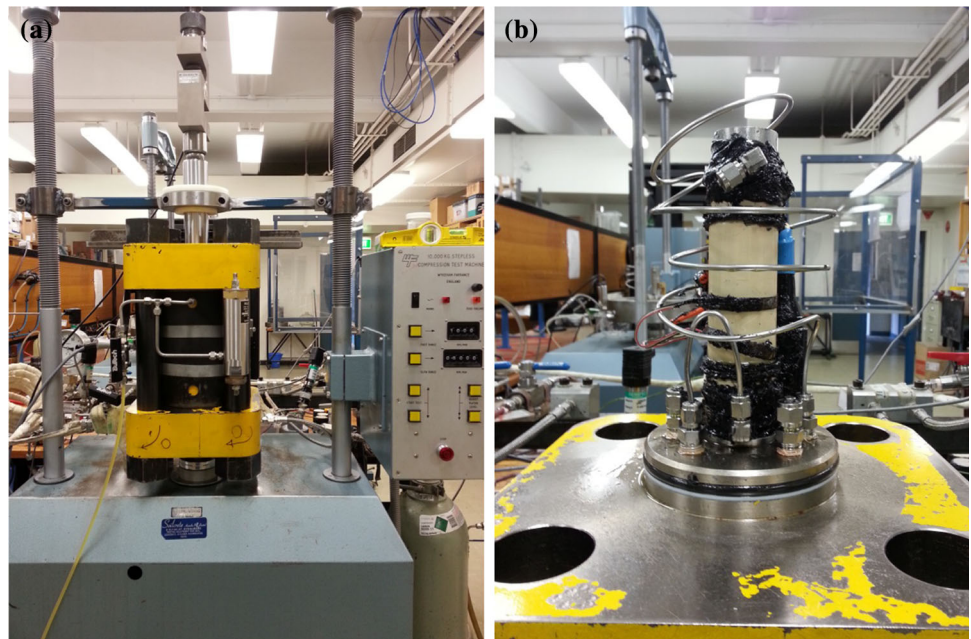
Permeability tests were performed using the high-pressure tri-axial rig available in the Deep Earth Energy Laboratory at Monash University. The setup (see Fig. 3a) can deliver injection pressures up to 50 MPa, confining pressures up to 70 MPa, axial loads up to 100 kN and temperatures up to 70 °C. The schematic diagram of the experimental setup is shown in Fig. 2, and a detailed description of this setup can be found in Ranjith and Perera (2011). Before placing the sample in the tri-axial cell, it was covered by a 2 mm thick and 37.5 mm internal diameter nitrile membrane to prevent oil leakage into the sample and CO₂ leakage into the oil.

Fig. 2 Schematic diagram of the experimental setup



☒	Pressure Transducer (PT)
○	Bolt Valve (BV)
∩	Needle Valve (NV)
∅	Pressure Gauge (PG)
⊘	Check Valve (CV)
⌈	Pressure Regulator (PR)
△	Relief Valve (RV)

Fig. 3 a The high-pressure tri-axial setup, **b** the sample after applying the silicon



The prepared sample was then placed in the tri-axial pressure cell and silicon sealing was applied over the boundaries between the top edge of the membrane and the top platen and bottom edge of the membrane and the bottom platen to minimize leakage (Fig. 3b).

After placing the sample, the cell was filled with oil and the required confining pressure was applied using a syringe pump with 50 MPa capacity. 20 MPa was selected as the confining pressure for the present study to represent the in situ stress condition at 1 km depth, assuming the density

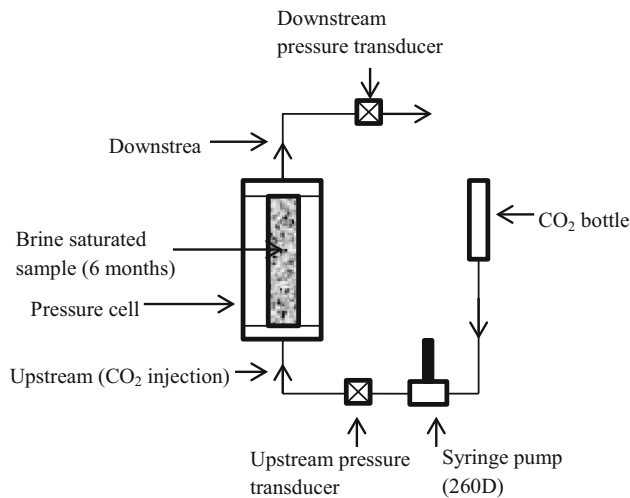


Fig. 4 Schematic diagram of CO₂ injection procedure

of sandstone is 2,000 kg/m³. When the desired confinement was reached the test temperature was set to 35 °C and the sample was allowed to heat for 24 h. CO₂ injection was conducted for both sub-critical and super-critical conditions.

After obtaining the required confinement, CO₂ was injected into the sample at constant injection pressure using a syringe pump (capacity of 260 D) and the downstream pressure development was recorded for the effective permeability calculation. The pressure values of the sample inlet and outlet were monitored using pressure transducers mounted across the upstream and downstream of the system. Figure 4 below shows the schematic diagram of the CO₂ injection procedure. The permeability tests were conducted under undrained conditions and the permeability calculation was done using the measured downstream pressure development curve and pressure transient approach was used. Each permeability test was completed within around 8 min and the system temperature was maintained at a constant 35 °C during each experiment. The overall test conditions are shown in Table 2.

As shown in Table 2, CO₂ was first injected into the water-saturated samples at 2 MPa constant injection pressure and the corresponding downstream pressure development was recorded for effective permeability

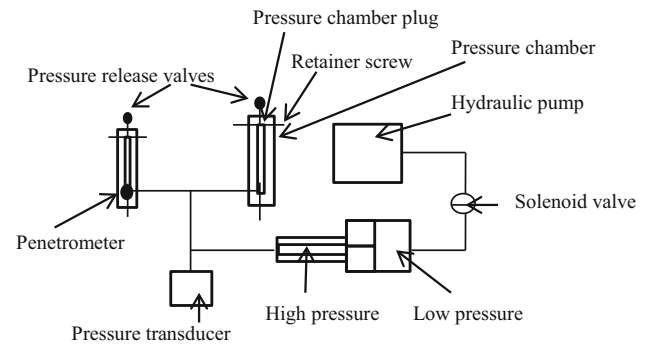


Fig. 5 Schematic diagram of high-pressure instrument used for MIP tests

calculation under this injection condition. After the downstream reached a steady-state pressure condition, downstream was opened and the downstream pressure was released before the subsequent injection. CO₂ was then injected at 4 MPa higher (constant) injection pressure, following the same procedure. The same procedure was repeated for 6, 8, 10, and 12 MPa injection pressures for the water-saturated samples. After testing the water-saturated samples, brine-saturated samples were tested in a similar way, and 10, 20, and 30 % NaCl brine-saturated samples were tested for the same injection pressures. Here, the injection pressures were selected considering the safety of the process (to prevent hydrofracturing), and the injection pressure was not allowed to exceed 90 % of the confining pressure to prevent the re-activation of joints or CO₂ leakage through the membrane and the specimens.

3.3 Porosity Measurement of Tested Samples

The porosity of the rock mass indicates its available pore space and is therefore important in fluid flow movement analysis. The porosity of the sandstone tested under each saturated condition was determined using mercury intrusion porosimetry (MIP) tests (Cnudde et al. 2009; Molina et al. 2011). The test was conducted in scanning mode and a continuously increasing pressure was applied to obtain the extrusion curve (Fig. 6), which was used to predict the sample's porosity. Figure 5 shows the schematic diagram

Table 2 Summary of tested saturation conditions and injection pressures

Saturation mediums	Number of replicates	Injection pressures (MPa)					
		2	4	6	8	10	12
Water saturated	2	2	4	6	8	10	12
10 % NaCl brine saturated	2	2	4	6	8	10	12
20 % NaCl brine saturated	2	2	4	6	8	10	12
30 % NaCl brine saturated	2	2	4	6	8	10	12

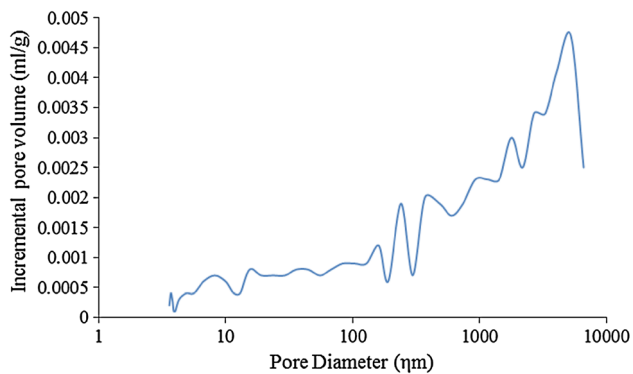


Fig. 6 Cumulative intrusion versus pore diameter curve derived by scanning (dry sample)

of the high-pressure instrument with a maximum pressure of 60,000 psi. The pressure was gradually increased from 1.6 psi to 60,000 psi in 117 steps, to measure the sample's pore volume, if the sample pore apertures ranged from ~ 140 to ~ 0.0036 microns in diameter.

To briefly describe the test procedure, the rock sample is first placed in the penetrometer, which holds a known amount of mercury at the beginning of the test. The penetrometer is initially filled with mercury at a pre-set filling pressure, and is then subjected to several pressure reduction steps, up to around 26 psi. It is then transferred to a high-pressure cell to complete the mercury injection at 60,000 psi pressure. During the high-pressure phase, the penetrometer is immersed in an oil bath (pressure transfer fluid) inside a steel pressure vessel. Increased oil pressure in the vessel causes the mercury to push into the sample and the position of the mercury meniscus in the penetrometer stem is read by capacitance. The data from the penetrometer, the low pressure, and high-pressure modes and the intrusion conditions used for the present study are shown in Table 3. The derived cumulative intrusion versus pore diameter curve using scanning mode, for the dry sample, is shown in Fig. 6.

4 Results and Discussion

In this study, water- and brine-saturated samples were selected to inject CO_2 under undrained conditions, assuming that injected CO_2 behaves as a laminar flow. This was confirmed by plotting the variation of CO_2 flow rate with the injection pressure (Fig. 7). According to Fig. 7, the CO_2 flow rate shows a linear relationship with injection pressure, which explains the applicability of Darcy's equation to find the effective CO_2 permeability in the rock samples under the conditions considered in this study.

Table 3 Summary of penetrometer, low pressure, high-pressure modes, and summary of intrusion data

Penetrometer:

Pen. constant: 10.683 $\mu\text{l/pF}$
 Pen. weight: 63.4358 g Rec.
 Stem volume: 0.3920 ml
 Max. head pressure: 4.4500 psia
 Pen. volume: 5.9723 ml
 Contact angle: 130.000°
 Adv. contact angle: 130.000°
 Hg surface tension: 485.000 dynes/cm
 Hg density: 13.5335 g/ml

Low pressure:

Evacuation pressure: 50.000 μmHg
 Evacuation time: 30 min
 Mercury filling pressure: 0.62 psia
 Equilibration time: 10 s
 Maximum intrusion volume: 100.000 ml/g

High pressure:

Equilibration time: 10 s
 Maximum intrusion volume: 100.000 ml/g
 No blank correction

Intrusion data summary

Total intrusion volume = 0.1717 ml/g
 Total pore area = 127.370 m^2/g
 Median pore diameter (volume) = 3.7 nm
 Median pore diameter (area) = 3.8 nm
 Average pore diameter (4 V/A) = 5.4 nm
 Bulk density = 2.1684 g/ml
 Apparent (skeletal) density = 3.4551 g/ml
 Stem volume used = 71 %

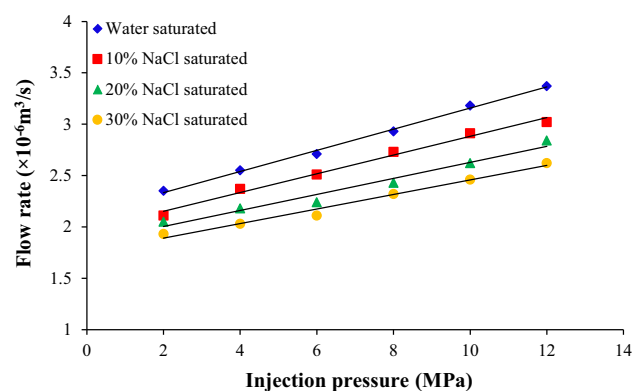
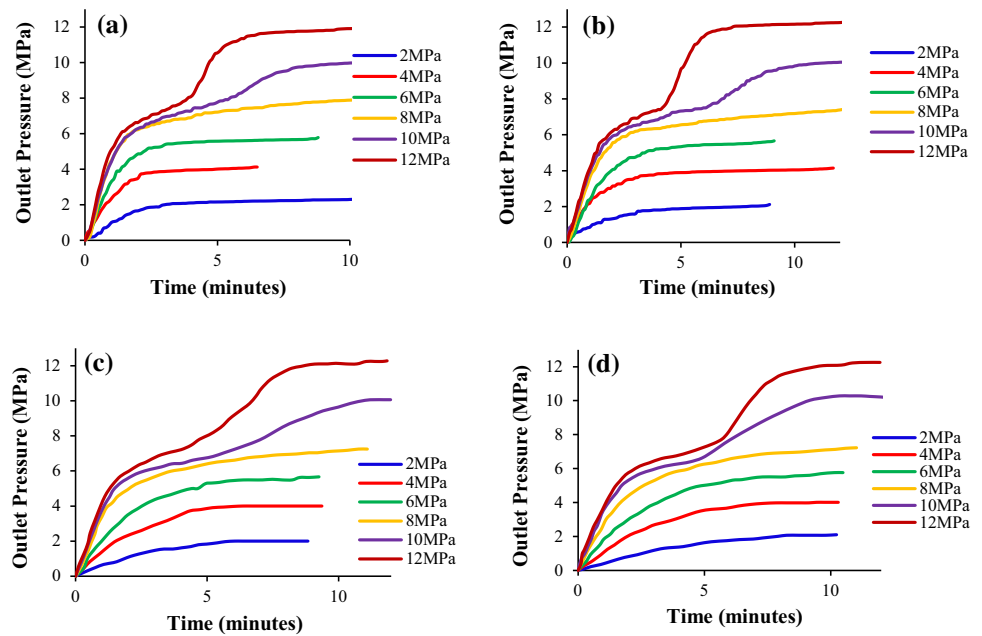


Fig. 7 Observed variation of flow rate with injection pressure for each saturation condition (confining pressure = 20 MPa)

The observed downstream pressure developments for each saturation condition are shown in Fig. 8. It is worth mentioning that the time required for outlet pressure to reach

Fig. 8 Observed downstream pressure developments for each saturation condition **a** water, **b** 10 % NaCl, **c** 20 % NaCl, and **d** 30 % NaCl-saturated samples



equilibrium increases with increasing salinity in the pore fluid. For example, at 12 MPa injection pressure, water-saturated samples took approximately 5 min to reach equilibrium, which then took nearly 6–8 min with the increase of salinity from 10 to 30 %. Interestingly, according to Fig. 8, there is a different downstream pressure development trend for higher CO₂ injection pressures (>8 MPa) compared to low pressures. This is mainly due to the higher pushing force created by the higher advective flux made by the higher injection pressure (the rate of the advective flux proportionally increases with the pressure gap between the upstream and downstream). This force causes inter-granular bonds to be weak, and this weakening effect gradually increases with time due to the continuously applied pushing force by the injection pressure creating advective flux. Eventually, the loosened bonds start to break at one stage of the injection, at which point a considerable amount of fine aggregates will be separated from the rock matrix and released to the downstream. This causes a sudden increase in rock mass pore space and eventually reduced tortuosity in the rock mass, resulting in quicker CO₂ mass flow rate toward downstream, resulting in the observed sudden downstream pressure development. In addition, according to Shukla (2011), the previously explained pushing force at high injection pressures causes CO₂ molecules to travel along preferential flow paths at the beginning of the injection as the pressure gap is higher at the beginning, resulting in the observed primary pressure development. This is believed to occur before the saturation of the whole rock mass. However, once the rock mass is totally saturated, this effect of preferential flow path will be replaced as now CO₂ movement can occur through the whole pore space of the rock mass. This effect may also partially contribute to the observed unique

pressure development trend at higher injection pressures. The temporal change in pressure was then used to calculate the gas flow rate through the reservoir rock using the following equation for a selected time period (Siriwardane et al. 2009; Perera et al. 2011).

$$Q = \left(\frac{dP}{dt} \right) \beta V \quad (13)$$

where, Q is the downstream flow rate, $\frac{dP}{dt}$ is the pressure gradient developed downstream, V is the downstream volume and β is the adiabatic compressibility of the pore fluid. The CO₂ permeability of the reservoir rock for each condition was then calculated using the Darcy equation (Monlouis-Bonnaire et al. 2004; Jasinge et al. 2011; Perera et al. 2011).

$$k = \frac{2QP_0\mu L}{A(P_i^2 - P_0^2)} \quad (14)$$

where Q , μ , P_0 , P_i , A , L , and k are the downstream flow rate, the viscosity of the pore fluid, the downstream pressure, the upstream pressure, the sample cross-sectional area, the sample length, and the initial permeability of the sample. The adiabatic compressibility and viscosity of CO₂ depend on the pressure and temperature values (Fenghou et al. 1998). Therefore, the REFPROP database was used to calculate the adiabatic compressibility and the viscosity of the CO₂ employed during the test (Table 4).

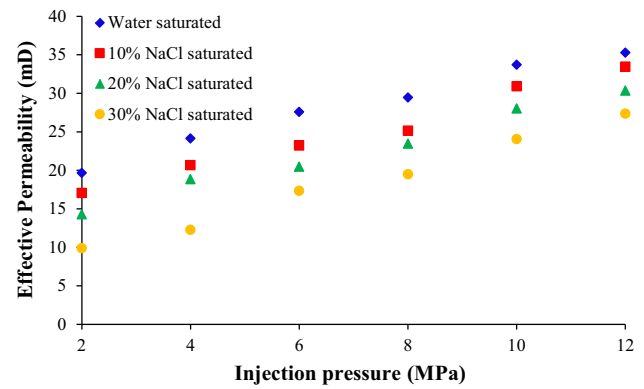
4.1 Effect of Salinity on Effective CO₂ Permeability

The degree of salinity is one of the critical considerations in deep saline sequestration studies, and it is found to

Table 4 Adiabatic compressibility and viscosity values obtained from REFPROP at different mean injection pressures

Temperature	Average injection pressure (MPa)	Adiabatic compressibility (MPa ⁻¹)	Viscosity (μMPas)
35 °C	0.25	2.867	1.56E-11
	1.15	0.67968	1.57E-11
	2	0.41451	1.58E-11
	2.25	0.34991	1.59E-11
	2.75	0.28657	1.6E-11
	3	0.36275	1.6E-11
	3.65	0.21588	1.63E-11
	4.7	0.16685	1.68E-11
	6.5	0.11624	1.85E-11

increase with increasing depth of the aquifer. It is therefore important to understand the effect of salinity on both the mechanical and permeability characteristics of reservoir rock to identify the most preferable aquifers for sequestration before initiating the process. Therefore, based on the experimental results, the effect of salinity on the effective CO₂ permeability of Hawkesbury sandstone is discussed in this section. According to past studies (Odeh 1959; Bennion and Bachu 2005; Bachu and Bennion 2008), among the various factors for the effective CO₂ permeability of sandstone in CO₂-brine systems (injection and confining pressures, temperature, IFT, viscosity ratio, capillary pressure, and degree of saturation), IFT has a significant effect on the displacement characteristics of CO₂-brine systems during the CO₂ injection phase (Bachu and Bennion 2008). Bachu and Bennion (2008) conducted a comprehensive experimental study to investigate the effect of IFT between CO₂ and brine on the effective permeability characteristics of reservoir rock, and found that the effective CO₂ permeability decreases with increasing IFT. This IFT mainly depends on the pressure, temperature, and brine salinity, and it increases with increasing temperature and salinity and decreasing injection pressure (Yang et al. 2005; Chalbaud et al. 2006). According to Bennion and Bachu (2006c), the viscosity ratio between CO₂ and brine may also play a considerable role in governing fluid movement through the CO₂-brine system, and increasing the viscosity contrast between CO₂ and brine causes more easy CO₂ movement. Figure 9 below shows the relationship between CO₂ injection pressure and effective CO₂ permeability of the rock samples tested under different salinity conditions. Here, water-saturated samples were used as benchmarks to identify the pure brine effect on the effective CO₂ permeability of reservoir rock. According to Figs. 9 and 10, it is clear that the effective CO₂ permeability of reservoir rock increases with increasing injection pressure and decreasing NaCl

**Fig. 9** Relationship between CO₂ injection pressure and the effective CO₂ permeability of reservoir rock under different salinity conditions (confining pressure = 20 MPa)

concentration of the pore fluid, and the effective CO₂ permeability values for 10 % NaCl-saturated samples at 2, 4, 6, 8, 10, and 12 MPa injection pressures are 17.046, 20.662, 23.218, 25.148, 30.919, and 33.465 mD, respectively. Therefore, effective CO₂ permeability in 10 % NaCl-saturated samples increases by around 96.32 % when the injection pressure is increased from 2 to 12 MPa. Similar trends were observed for both 20 and 30 % NaCl-saturated samples, where effective CO₂ permeability increases from 14.27 to 30.35 mD in 20 % NaCl-saturated samples and from 9.88 to 27.35 mD in 30 % NaCl-saturated samples with 2 to 12 MPa CO₂ injection pressure increments (Table 5). The observed effective CO₂ permeability increments with increasing injection pressures mainly relate to the effective stress effect, where increased injection pressure causes the rock mass pore pressure to increase, resulting in reduced effective stress. Effective stress is the parameter which exhibits the effect of external stress on any rock mass, and its reduction causes the rock mass to expand by increasing its pore space. This eventually reduces the rock mass tortuosity for CO₂ movement, resulting in enhanced permeability in the rock mass. Apart from this, increasing injection pressure creates higher advective flux through the rock mass, and the higher pushing force created by this flux enhances the force applied on inter-aggregate bonds and eventually extracts fine particles from the rock mass. This also influences the permeability enhancement, because fine particles always obstruct the fluid flow path in the rock mass by creating a closer packing arrangement between aggregates. The removal of at least some of them should create better flow paths for CO₂ movement, resulting in enhanced permeability in the rock mass. Moreover, according to Yang et al. (2005), IFT between CO₂ and brine strongly depends on injection pressure, and it decreases with increasing injection pressure, resulting in increased effective CO₂

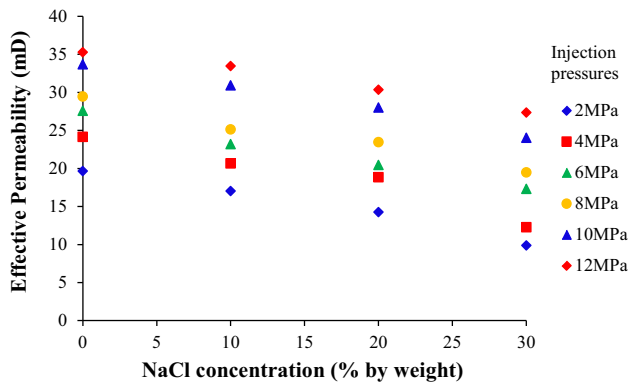


Fig. 10 Relationship between salinity and the CO₂ permeability of reservoir rock under different CO₂ injection pressures (confining pressure = 20 MPa)

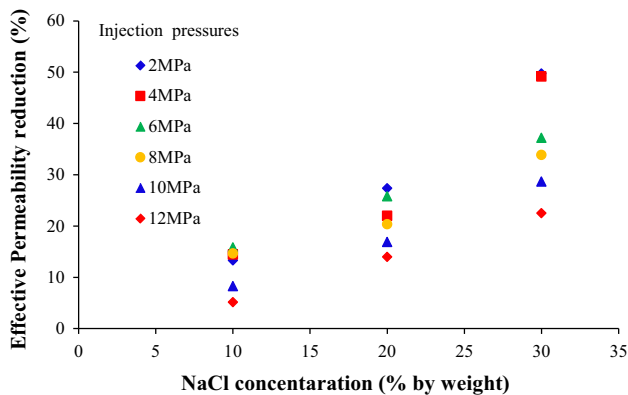


Fig. 11 Relationship between salinity and the reduction of effective CO₂ permeability compared to water saturation (confining pressure = 20 MPa)

permeability as IFT always creates a negative influence on the CO₂ migration through the rock mass. If the salinity effect on effective CO₂ permeability is considered, as can be seen in Fig. 10, effective CO₂ permeability exhibits a decreasing trend with increasing salinity at each injection pressure. Figure 11 and Table 5 below show the observed reduction in effective CO₂ permeability compared to water-saturated values. According to these results, at 2 MPa injection pressure, significant reductions of 13.28, 27.38, and 49.74 % in effective CO₂ permeability were observed in 10, 20, and 30 % NaCl-saturated samples compared to water-saturated samples. However, there was a clear reduction in permeability with increasing injection pressures from 2 to 12 MPa, with around 5.16, 13.99, and 22.49 % reductions in permeability being observed in 10, 20, and 30 % NaCl-saturated samples at 12 MPa injection pressure compared to water-saturated samples. The permeability reductions are clearly significant at low injection pressures compared to high injection pressures for each

Table 5 Summary of calculated permeability values and permeability reduction compared to water-saturated specimens

Saturation medium	Injection pressures	CO ₂ permeability (mD)	Permeability reduction (%) compared to water saturation
Water	2	19.657	
	4	24.147	
	6	27.581	
	8	29.459	
	10	33.71	
	12	35.284	
10 %	2	17.046	13.28
	4	20.662	14.42
	6	23.218	15.82
	8	25.148	14.63
	10	30.919	8.27
	12	33.465	5.15
20 %	2	14.274	27.38
	4	18.838	21.98
	6	20.462	25.81
	8	23.465	20.34
	10	28.02	16.88
	12	30.346	13.99
30 %	2	9.879	49.74
	4	12.273	49.17
	6	17.318	37.21
	8	19.479	33.87
	10	24.040	28.68
	12	27.350	22.48

tested condition due to the high effective stress applied on the rock mass at low injection pressure. According to Yang et al. (2005) and Chalbaud et al. (2006), IFT between CO₂ and brine depends on pore fluid salinity, and IFT increases with increasing salinity, resulting in reduced effective CO₂ permeability in the system. In addition, according to Bennion and Bachu (2006c), the viscosity ratio between the two fluids may also play a considerable role in governing the fluid movement behavior in the CO₂-brine system, where the fluid movement through the pore space becomes much easier (increases) at increased viscosity contrast between CO₂ and brine. Increasing the salinity causes the brine viscosity to increase, which therefore, enhances the viscosity gap between the CO₂ and brine. According to the explanation of Bennion and Bachu (2006c), this should create a positive influence on the CO₂ movement in brine or effective CO₂ permeability in brine that is in contrast to the observed permeability reduction at increased NaCl concentration in brine. However, according to Bachu and Bennion (2008), the effect of the viscosity ratio between brine and CO₂ is less significant compared to the effect of

IFT between brine and CO₂ on the effective permeability of reservoir rock. This explains the decreased effective CO₂ permeability at higher salinity conditions. In addition, there is a possibility of NaCl crystallization in the rock pore space during long-term brine saturation conditions, which is a further possible reason for the effective CO₂ permeability reduction observed with increasing salinity in the pore fluid. It should be noted that here each sample was saturated in brine with various concentrations (0, 10, 20, and 30) for 6 months before starting the permeability tests, and interaction between the brine and rock mass during such long time period causes the NaCl in brine to be crystallized in the rock mass pore space and increasing the NaCl concentration in the pore fluid offers more opportunity for the crystallization process. Effective permeability reduction with increasing NaCl concentration has been seen by other researchers (Shukla et al. 2012; Rathnaweera et al. 2014) and according to them, NaCl crystals are deposited in the rock pore structure as a result of long-term exposure of rock mass to highly saline brine.

In addition to this permeability analysis (pressure transient method), data on porosity from the MIP tests were also used to evaluate the effective CO₂ permeability in brine-saturated reservoir rock samples (Eq. 1). This analysis can be used to confirm the accuracy of the experimental results and also to confirm the influence of the suspected pore structure variation on rock sample permeability under various injection conditions, including injection pressure, effective confining pressure, and NaCl concentration in the pore fluid. To perform the MIP test, a small portion of sandstone was extracted from the sample, after finishing the permeability testing under each test condition (different injection and confining pressures and salinity), and the effects of effective confining pressure and degree of salinity on the sandstone sample's porosity were investigated. The porosity values were then used to determine the effective CO₂ permeability of sandstone under the tested condition and this value was compared with the values obtained from the experiments. According to the comparison, the values obtained from the two methods are mostly similar, with a standard deviation around 0.032, which confirms the accuracy of the experimental results.

Figure 12 shows porosity variation with injection pressure for each brine saturation condition. According to the figure, porosity increases with increasing injection pressure (from 2 to 12 MPa), probably due to the reduction of effective confining pressure with injection pressure increment, which eventually expands the pore space of the rock sample. In addition, Fig. 12 shows a trend of reduction of reservoir rock porosity with increasing NaCl concentration in the pore fluid (from 10 to 30 %), regardless of injection pressure. This is believed to be related to the NaCl

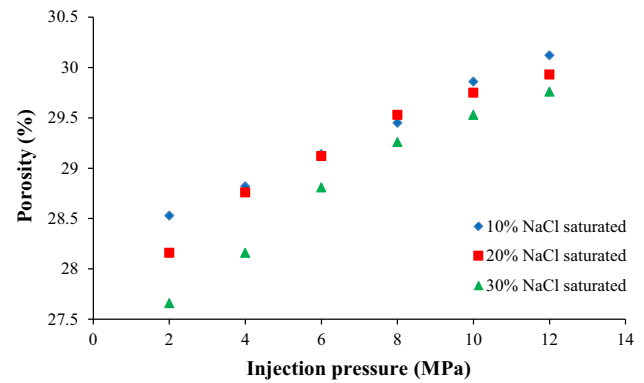


Fig. 12 Relationship between porosity and the injection pressure in 10, 20, and 30 % concentration of NaCl-saturated samples (confining pressure = 20 MPa)

crystallization process in the rock mass pore space. The occupation of the existing pore space by the NaCl crystals causes the pore space to be reduced. Increasing the NaCl concentration in the pore fluid offers more opportunity for the NaCl crystallization process, resulting in reduced porosity at higher NaCl concentrations in the pore fluid. This NaCl crystallization process-induced porosity reduction was then confirmed by performing SEM analyses (Fig. 13) on variably saturated rock samples (at different NaCl concentrations of 10, 20, and 30 % NaCl). These findings are fairly consistent with the findings on the experimental permeability data and, therefore, prove the validity of the pore structure variation argument to describe the influence of injection and confining pressures and NaCl concentration in the pore fluid on reservoir effective permeability.

Figure 14 shows the comparison of results for effective CO₂ permeability values from this method and the previously mentioned pressure transient analysis. According to the results, both methods are in good agreement in evaluating effective CO₂ permeability in brine-saturated reservoir rock samples.

Considering these findings, SEM and chemical analysis were then performed to identify the physical phenomena behind this observed permeability reduction with increasing salinity. The results are discussed in Sect. 4.4.

4.2 Influence of Effective Stress on Effective CO₂ Permeability in Brine-Saturated Sandstone

According to past studies, it is clear that permeability is dependent on effective stress, and permeability decreases as effective hydrostatic pressure is increased (Keaney et al. 2004). Effective pressure can be defined as $P_{\text{eff}} = P_{\text{con}} - P_{\text{flu}}$, where P_{eff} is the effective confining pressure, P_{con} is the confining pressure, and P_{flu} is the fluid pressure.

Fig. 13 SEM images of NaCl crystals deposited in the rock pore space during 6 months saturation

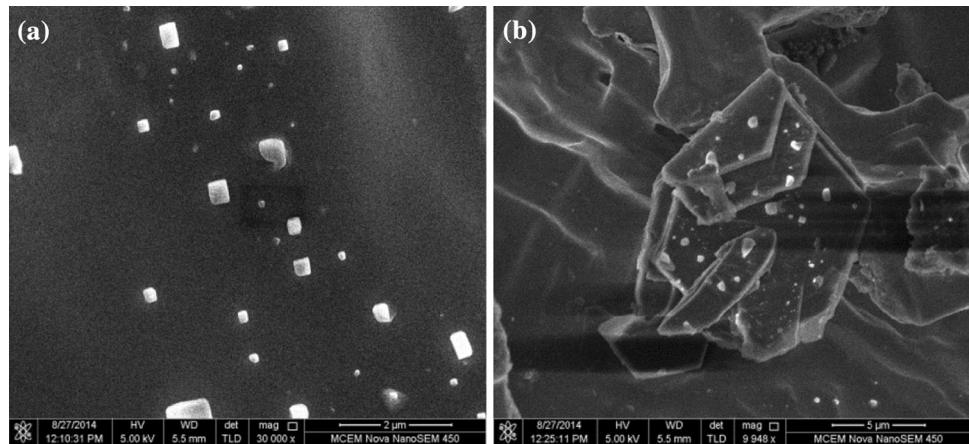


Figure 15 shows the effective CO₂ permeability of the sandstone samples as a function of effective confining pressure for different saturation conditions. According to Fig. 15, it is clear that effective CO₂ permeability decreases as the effective confining pressure is increased from 8 to 18 MPa for all the saturation conditions. In water-saturated specimens, a reduction of 36.92 % in effective CO₂ permeability was observed by increasing the effective confining pressure from 8 to 18 MPa. Furthermore, reductions of 49.12, 60.92, and 69.92 % in effective CO₂ permeability were observed as the effective confining pressure was increased from 8 to 18 MPa in 10, 20, and 30 % NaCl-saturated samples, respectively. This observed reduction in effective CO₂ permeability (see Fig. 15) is due to the shrinkage of the rock mass caused by increased effective confining stress, which consequently reduces the effective fluid pathway connectivity in the pore structure. Moreover, the observed reduction in effective confining pressure with increasing CO₂ injection pressure causes the effective CO₂ permeability to be increased in water- and brine-saturated samples. The shrinkage effect reduces with decreasing effective confining pressure in the rock pore structure and consequently increases the effective pore space for CO₂ migration along the sample. This may be the reason for the effective CO₂ permeability increments observed with increasing injection pressures in water- and brine-saturated samples. In addition, fine particle migration (particle rearrangement) increases with increasing injection pressure, which also enhances the free path of gas flow and consequently increases the effective CO₂ permeability of reservoir rock. Moreover, according to Yang et al. (2005), IFT between CO₂ and brine strongly depends on injection pressure, and it decreases with increasing injection pressure, resulting in increased effective CO₂ permeability, as IFT always creates a negative influence on the CO₂ migration through the rock mass.

In addition, for a certain effective confining pressure, effective CO₂ permeability decreases with increasing

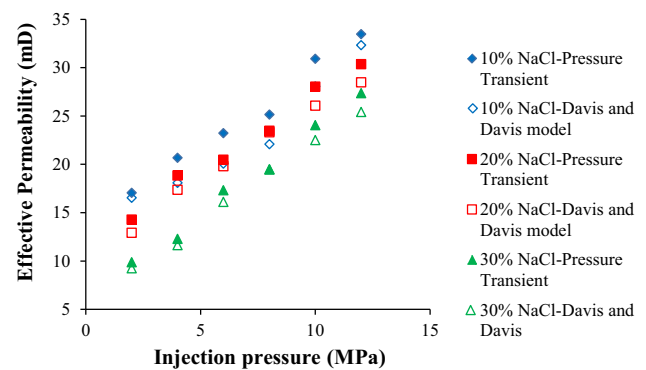


Fig. 14 Comparison between pressure transient permeability evaluation and Davies and Davies (1999) permeability model (confining pressure = 20 MPa)

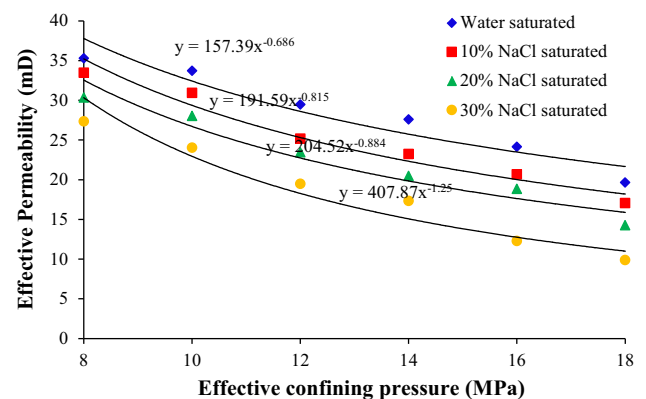


Fig. 15 Effective CO₂ permeability as a function of effective confining pressure for different saturation conditions compared to water saturation

salinity in the pore fluid from 0 to 30 % NaCl, which may be related to the crystallization process of NaCl in the pore structure, where deposited crystals reduce the free flow paths for CO₂. Increasing salinity causes this crystal growth to be enhanced.

4.3 The Klinkenberg Effect

The variation of effective CO₂ permeability in reservoir rock under dry (CO₂ permeability), water-, 10, 20, and 30 % brine-saturated conditions with different injection pressures is shown in Fig. 16. As Fig. 16 shows, CO₂ permeability in dry reservoir rock reduces with increasing injection pressure, and a similar trend has been observed by Nasvi et al. (2013) for dry geo-polymer samples. In contrast, an increasing trend of effective CO₂ permeability with increased injection pressure can be seen in wet samples (water-saturated and brine-saturated). These opposite permeability behaviors of CO₂ in dry and wet sandstones may be related to Klinkenberg effect (Abbas et al. 1999; Loosveldt et al. 2002; Picandet et al. 2009). According to existing studies, gas permeability through porous rocks reduces with increasing injection pressure due to Klinkenberg effect (Abbas et al. 1999; Loosveldt et al. 2002; Picandet et al. 2009). As described in Sect. 2.3, the permeability of any porous medium to gas is relatively higher

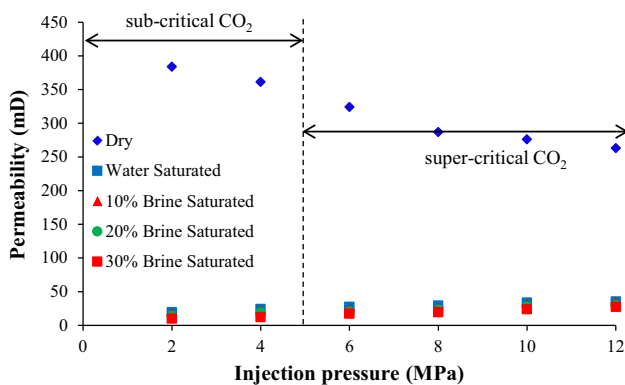


Fig. 16 Variation of effective CO₂ permeability in reservoir rock under dry, water, 10, 20, and 30 % brine-saturated conditions at different injection pressures (confining pressure = 20 MPa)

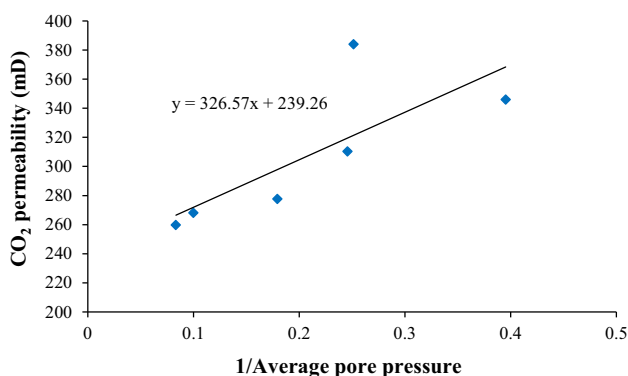


Fig. 17 Variation of CO₂ permeability in dry sample against the inverse of the average pore pressure (confining pressure = 20 MPa)

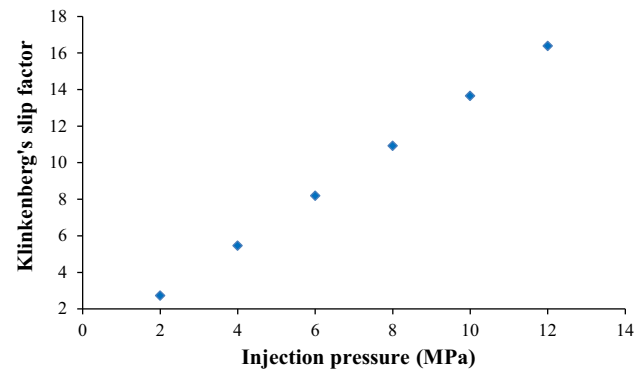


Fig. 18 Relationship between Klinkenberg slip factor and the injection pressure (confining pressure = 20 MPa)

than water due to the slip flow effect, which leads to the creation of an additional flux, and consequently increases the flow rate (Tanikawa and Shimamoto 2009). This explains the observed permeability behavior in the dry samples, which show a reduction of effective CO₂ permeability from 383.9 to 330.23 mD with the increase of injection pressure from 2 to 6 MPa (13.98 % reduction of CO₂ permeability). Interestingly, more significant CO₂ permeability reduction is seen with the phase transition of the CO₂ from gas to super-critical state (6 MPa to 8 MPa at 35 °C), which is around a 21.99 % reduction, possibly due to the reduced slip flow effect at the super-critical state of CO₂. A further increase of CO₂ pressure (8 to 10 MPa) causes only a small permeability reduction (3.85 %). This is because the CO₂ is now in its super-critical condition and, therefore, further increase of pressure while keeping the temperature constant does not change its phase. Therefore, a minor slip flow effect can be expected.

If the permeability of the wet samples (water- and brine-saturated) is now considered, as a consequence of water/brine saturation, the frequency of collisions between the solid wall and mean gas molecules is decreased due to the friction between water and gas phases, resulting in a reduced slip flow effect. Therefore, the observed permeability reduction trend is mainly related to the pressure-dependent brine/water migration phenomenon, where the migration process increases with increasing injection pressure (due to reduced effective stress), resulting in increased rock permeability. In addition, a small amount of injected CO₂ may also dissolve in brine/water, depending on the CO₂ concentration. Overall, it can be said that the gas and super-critical effective CO₂ permeability values of water/brine-saturated samples do not differ greatly from those of dry samples.

In addition, the CO₂ permeability data of dry samples were used to determine the Klinkenberg slip factor. The CO₂ permeability data were plotted against the inverse of the average pore pressure, and the average pore pressure

Table 6 Amount of NaCl deposition from chemical analysis

	Water	10 % NaCl saturated	20 % NaCl saturated	30 % NaCl saturated
Amount of NaCl (ppm)	731	18,251	41,433	61,712

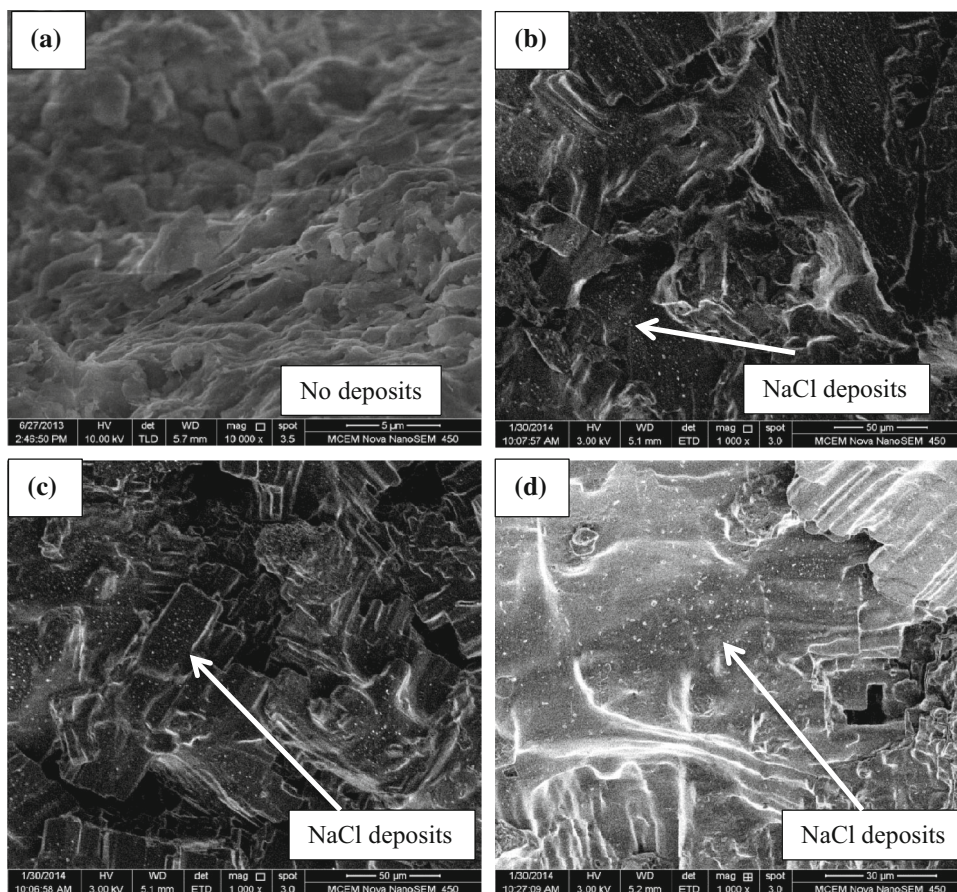
was calculated by finding the average of the inlet and outlet CO₂ injection pressures (Fig. 17). According to the test results, the CO₂ permeability increases linearly as the inverse of pore pressure increased. Interestingly, the Klinkenberg slip factor for dry Hawkesbury sandstone varies from 2.7 to 16.4 with increasing injection pressure from 2 to 12 MPa (Fig. 18).

4.4 The Corresponding Variations in the Rock Mineral Structure

To identify the variations observed in effective CO₂ permeability in reservoir rocks, a complete micro-structural analysis using SEM was performed (Fig. 19). The SEM analysis was conducted on a 0.3 mm thick sandstone slice taken from the sample prior to each experiment (after 6 months' saturation) under wet conditions. The slice was

then double-coated using Pt (3 mm platinum coating) to remove the charging effect during the image processing (scanning) stage. To obtain clear images of the sandstone topography, the voltage and spot size were selected to be 5.0 kV and 2.0–3.5, respectively. According to Fig. 19, there are significant depositions of NaCl crystals in the tested sandstones, which have been saturated in brine with 20 and 30 % NaCl concentrations, and only a minor deposition of NaCl crystals in sandstone saturated in brine with 10 % NaCl. This NaCl crystallization process occurred during the long-term saturation (6 months) of sandstone in brine. Although the amount of NaCl crystallized might not be exactly similar to the real field situation (crystallization occurs under high pressure and temperature conditions in the field), the trend is believed to be similar. A detailed chemical analysis was then conducted to identify the amount of NaCl deposition in the rock pore space under each brine saturation condition (water, 10, 20, and 30 % NaCl concentrations). This was achieved by stirring a weighted quantity of sample in de-mineralized water, filtering this water and analyzing the solution for Na and Cl. The analysis was conducted on a small sandstone slice taken from each tested sample prior to conducting the permeability experiments (after 6 months saturation in

Fig. 19 SEM analysis results of **a** water, **b** 10 % NaCl, **c** 20 % NaCl, and **d** 30 % NaCl-saturated specimens



water, 10, 20, and 30 % NaCl concentrations). According to the analysis (Table 6), the NaCl concentration in water-saturated samples, 731 ppm, increases up to 18,251, 41,433, and 61,712 ppm due to the presence of 10, 20, and 30 % NaCl (brines), which confirms the increment of salt deposition in rock mass with increasing NaCl concentration. Although the result is not precise, as there are many soluble compounds present in the sample and Na is ubiquitous, the trend should be correct. Therefore, this analysis is believed to be a good indication of the effect of NaCl concentration in brine on the NaCl crystallization process in sandstone.

According to the permeability analysis, 10, 20, and 30 % of NaCl saturation caused the reservoir rock's permeability to be reduced by 5, 15, and 22 % at low effective confining pressures (pressure range of 8–10 MPa) and 13, 27, and 50 % at high effective confining pressures (pressure range of 16–18 MPa), respectively, compared to water-saturated samples. This permeability reduction in the rock specimens appears to be clearly related to the NaCl crystallization process in the rock pore spaces, where the crystals deposited in the rock pore space block the free flow CO₂ paths, resulting in reduction of effective CO₂ permeability.

5 Conclusions

carbon dioxide sequestration in deep saline aquifers is a promising solution to reducing the anthropogenic emissions of CO₂ into the atmosphere. However, the permeability variation with effective stress and salinity add many complications to the sequestration process. A compressive study was, therefore, conducted to identify the effect of salinity on aquifer effective CO₂ permeability for a range of salinities (0, 10, 20, and 30 % NaCl) using a series of high-pressure tri-axial permeability tests. The following major conclusions can be drawn:

- The presence of NaCl in pore fluid causes the reservoir rock's permeability to be reduced and this effect increases with increasing NaCl saturation in the pore fluid. For example, at low injection pressures (2–6 MPa), 13, 27, and 50 % effective permeability reductions were observed in 10, 20, and 30 % brine-saturated specimens compared to water-saturated specimens. At high injection pressures (10–12 MPa), 5, 14, and 23 % effective permeability reductions were observed in 10, 20, and 30 % brine-saturated specimens compared to water-saturated samples.
- According to a comprehensive chemical analysis, when the pore fluid has a higher degree of salinity, there are considerable numbers of NaCl crystals in the pore structure, which reduces the reservoir effective permeability by obstructing the flow paths.
- Effective CO₂ permeability of reservoir rock increases with increasing injection pressure in wet (water/brine-saturated) samples for a given confining pressure, due to the effective stress reduction.
- In contrast, CO₂ permeability reduces with increased injection pressure for dry samples, due to Klinkenberg effect.

References

- Abbas A, Carcasses M, Ollivier JP (1999) Gas permeability of concrete in relation to its degree of saturation. *Mater Struct* 32:3–8
- Aktan T, Farouk ASM (1975) Effect of cyclic and in situ heating on the absolute permeabilities, elastic constants and electrical resistivities of rocks. Presented at the 50th Annual Fall Meeting of the SPE of AIME, Dallas, TX SPE, 5633:1–10
- Arsyad A, Mitani Y, Babadagli T (2013) Comparative assessment of potential ground uplift induced by injection of CO₂ into Ainoura, and Berea sandstone formations. *Procedia Earth Planet Sci* 6:278–286
- Bachu S, Bennion B (2008) Effects of in situ conditions on relative permeability characteristics of CO₂-brine systems. *Environ Geol* 54(8):1707–1722
- Baudracco J, Tardy Y (1988) Dispersion and flocculation of clays in unconsolidated sandstone reservoirs subjected to percolation with NaCl and CaCl₂ solutions at different temperatures. *Appl Clay Sci* 3(4):347–360
- Bennion B, Bachu S. (2005). Relative permeability characteristics for CO₂ displacing water in a variety of potential sequestration zones in the Western Canada Sedimentary Basin. Paper SPE 95547, p 15, presented at the 2005 SPE Technical Conference and Exhibition, Dallas, TX, 9–12 October 2005 PAGES?
- Bennion B, Bachu S (2006c) Dependence on temperature, pressure and salinity of the IFT and relative permeability displacement characteristics of CO₂ injected in deep saline aquifers. Paper SPE 102138, p 10, presented at the 2006 SPE technical conference and exhibition, San Antonio, TX, 24–27 September : 120–133
- Bennion DB, Bachu S (2010) Drainage and imbibition CO₂/brine relative permeability curves at reservoir conditions for carbonate formations, in SPE Annual technical conference and exhibition, SPE 134028, pp 1–18, Society of Petroleum Engineers, Florence, Italy
- Berg S, Oedai S, Ott H (2013) Displacement and mass transfer between saturated and unsaturated CO₂-brine systems in sandstone. *Int J Greenh Gas Control* 12:478–492
- Biot MA (1941) General theory of three-dimensional consolidation. *J Appl Phys* 12(2):155–164
- Burton M, Kumar N, Bryant SL (2009) CO₂ injectivity into brine aquifers: why relative permeability matters as much as absolute permeability. *Energy Procedia* 1(1):3091–3098
- Chalabaud C, Robin M, Egermann P (2006) Interfacial tension of CO₂/brine systems at reservoirs conditions. In: Gale J, Rokke N, Zweigel P, Swenson H (eds) Proceedings of the 8th International Conference on Greenhouse Gas Control Technology, Elsevier, Amsterdam CD ROM
- Chen Y, Zhou C, Sheng Y (2007) Formulation of strain-dependent hydraulic conductivity for a fractured rock mass. *Int J Rock Mech Min Sci* 44(7):981–996

- Cnudde V, Cwirzen A, Masschaele B, Jacobs PJS (2009) Porosity and microstructural characterization of building stones and concretes. *Eng Geol* 103(3–4):76–83
- Dahab AE, El Omar, Gassier MM, Kariem HA (1992) Formation damage effects due to salinity, temperature and pressure in sandstone reservoirs as indicated by relative permeability measurements. *J Petrol Sci Eng* 6(4):403–412
- Davies JP, Davies DK (1999) Stress-dependent permeability: characterization and modeling. *Soc Pet Eng (SPE)*, Houston
- Dong JJ, Hsu JY, Wu WJ, Shimamoto T, Hung JH, Yeh EC et al (2010) Stress-dependence of the permeability and porosity of sandstone and shale from TCDP Hole-A. *Int J Rock Mech Min Sci* 47(7):1141–1157
- Faulkner D, Rutter E (2000) Comparisons of water and argon permeability in natural clay-bearing fault gouge under high pressure at 20 °C. *J Geophys Res Solid Earth* (1978–2012) 105(B7):16415–16426
- Fenghou A, Wakeham WA, Vesovic V (1998) The viscosity of carbon dioxide. *J Phys-Chem Ref Data* 27:31–44
- Hangx S, Van der Linden A, Marcellis F, Bauer A (2013) The effect of CO₂ on the mechanical properties of the Captain Sandstone: geological storage of CO₂ at the Goldeneye field (UK). *Int J Greenh Gas Control* 201:5–17
- Jasinge D, Ranjith PG, Choi SK (2011) Effects of effective stress changes on permeability of Latrobe Valley brown coal. *Fuel* 90(3):1292e 300
- Jing XD, Archer JS, Daltaban TS (1992) Laboratory study of the electrical and hydraulic properties of rocks under simulated reservoir conditions. *Mar Pet Geol* 9(2):115–127
- Juanes R, Spiteri EJ, Orr FM, Blunt MJ (2006) Impact of relative permeability hysteresis on geological CO₂ storage. *Water Resour Res* 42(12):32–41
- Julio GE (2001) Density of aqueous solutions of CO₂. Lawrence Berkeley National Laboratory. <http://escholarship.org/uc/item/6dn022hb>
- Keaney GM, Meredith P, Murrell S, Barker J (2004) Determination of the effective stress laws for permeability and specific storage in low porosity sandstone. Gulf Rocks 2004, the 6th North America rock mechanics Symposium (NARMS), 5–9 June, Texas, Houston, pp 24–36
- Khilar KC (1981) Water sensitivity of sandstone. Ph.D thesis, University of Michigan
- Klinkenberg L (1941) The permeability of porous media to liquids and gases. Drilling and production practice. American Petroleum Institute, New York, pp 21–34
- Kuhn M, Vernoux JF, Kellner T, Isenbeck-Schroter M, Schulz HD (1998) Onsite experimental simulation of brine injection into a clastic reservoir as applied to geothermal exploitation in Germany. *Appl Geochem* 13:477–490
- Leverett M (1940) Capillary behavior in porous solids. *Trans. Am. Inst. Pet Transp* 12:123–134
- Loosveldt H, Lafhaj Z, Skoczylas F (2002) Experimental study of gas and liquid permeability of a mortar. *Cem Concr Res* 32:1357–1363
- Miller MA, Ramey HJ (1986) Effect of temperature on oil/water relative permeability of unconsolidated sands. *J Pet Eng* 34:1945–1955
- Mohan KK, Reed MG, Fogler HS (1999) Formation damage in smectic sandstones by high ionic strength brines. *Colloids and surfaces A: physical and Chemical Engineering. Aspects* 154:249–257
- Molina E, Cultrone G, Sebastian E, Alonso FJ, Carrizo L, Gisbert J, Buj O (2011) The pore system of sedimentary rocks as a key factor in the durability of building materials. *Eng Geol* 118(3–4):110–121
- Monlouis-Bonnaire JP, Verdier J, Perrin B (2004) Prediction of the relative permeability to gas flow of cement-based materials. *Cement and Concrete Research* 34:737–744
- Nasvi MCM, Ranjith PG, Sanjayan J (2013) The permeability of geopolymer at down-hole stress conditions: application for carbon dioxide sequestration Wells. *Appl Energy* 102:1391–1398
- Neuzil CE (1994) How permeable are clays and shales? *Water Resour Res* 30(2):145–150
- Ochi J, Vernoux JF (1998) Permeability decrease in sandstone reservoirs by fluid injection: hydrodynamic and chemical effects. *J Hydrol* 208:237–248
- Odeh AS (1959) Effect of viscosity ratio on relative permeability. *Pet Transp AIME* 216:346–353
- Omar A (1990) Effect of brine composition and clay content on the permeability damage of sandstone cores. *J Pet Sci Eng* 4(3):245–256
- Pearce JM, Holloway S, Wacker H, Nelis MK, Rochelle C, Bateman K (1996) Natural occurrences as analogues for the geological disposal of carbon dioxide. *Energy Convers Manag* 37(6–8):1123–1128
- Perera MSA, Ranjith PG, Airey D, Choi SK (2011) Sub-critical and super-critical carbon dioxide flow behaviour in naturally fractured black coal: an experimental study. *J Fuel*. doi:10.1016/j.fuel.2011.05.016
- Picandet V, Khelidj A, Bellegou H (2009) Crack effects on gas and water permeability of concretes. *Cem Concr Res* 39:537–547
- Probst P (2008) Numerical simulations of CO₂ injection into saline aquifers: estimation of storage capacity and arrival times using multiple realizations of heterogeneous permeability fields. Master thesis, University of Stuttgart, German
- Ranjith PG, Perera MSA (2011) A new triaxial apparatus to study the mechanical and fluid flow aspects of carbon dioxide sequestration in geological formations. *Fuel* 90:2751–2759
- Ranjith PG, Perera MSA, Khan E (2013) A study of safe CO₂ storage capacity in saline aquifers: a numerical study. *Int J Energy Res* 37:189–199
- Rathnaweera TD, Ranjith PG, Perera MSA (2014) Salinity-dependent strength and stress-strain characteristics of reservoir rocks in deep saline aquifers: an experimental study. *Fuel* 122:1–11
- Rutqvist J, Tsang CF (2002) A study of caprock hydro-mechanical changes associated with CO₂-injection into a brine formation. *Environ Geol* 42:296–305
- Samuel CMK, Ronny P, Zuo L, Benson SM (2012) Relative permeability and trapping of CO₂ and water in sandstone rocks at reservoir conditions. *Water Resour Res* 48:w02532. doi:10.1029/2011wr010859
- Scheidegger AE (1958) The physics of flow through porous media. *Soil Sci* 86(6):355–342
- Shukla R (2011) Study of reservoir rock and caprock integrity in geo-sequestration of carbon dioxide. Ph. D. thesis. Monash University, Australia
- Shukla R, Ranjith PG, Choi SK, Haque A, Yellishetty M, Hong L (2012) Mechanical behaviour of reservoir rock under brine saturation. *Rock Mech Rock Eng* 46(1):83–89
- Siriwardane HJ, Gondle RK, Smith DH (2009) Influence of carbon dioxide on coal permeability determined by pressure transient methods. *Int J Coal Geol* 77(1):109–118
- Sydansk RD (1981) Discussion of the effect of temperature and confining pressure on single-phase flow in consolidated rocks. *J Pet Eng* 32:1329–1330
- Tanikawa W, Shimamoto T (2009) Comparison of Klinkenberg-corrected gas permeability and water permeability in sedimentary rocks. *Int J Rock Mech Min Sci* 46(2):229–238
- Vilarrasa V, Olivella S, Carrera J (2010) Geomechanical stability of the caprock during CO₂ sequestration in deep saline aquifers. *Energy* 4:5306–5313
- Wang HF (2000) Theory of linear poroelasticity: with applications to geomechanics and hydrogeology. Princeton University Press, Princeton

- Ward CR (1972) Sedimentation in the Narrabeen Group, southern Sydney basin, New South Wales. *J Geol Soc Australia* 19(3):393–409
- Wegener DC, Harpole KJ (2010) Determination of relative permeability and trapped gas saturation for predictions of WAG performance in the South Cowden CO₂ flood, in SPE/DOE tenth symposium on improved oil recovery, SPE 35429, Society of Petroleum Engineers, Tulsa, Oklahoma, pp 1–13
- White CU, Strazisar BR, Granite EJ, Hoffman JS, Pennline HW (2003) Separation and capture of CO₂ from large stationary sources and sequestration in geological formations—coalbeds and deep saline aquifers. *J Air Waste Manag Assoc* 53(6):645–715. doi:[10.1080/10473289.2003.10466206](https://doi.org/10.1080/10473289.2003.10466206)
- Yang D, Tontiwachwuthikul P, Gu Y (2005) Interfacial tensions of the crude oil + reservoir brine + CO₂ systems at pressures up to 31 MPA and temperatures of 27°C and 58°C. *J Chem Eng Data* 50:1242–1249